Analysis of Aerothermal Loads on Spherical Dome Protuberances

George C. Olsen* and R. E. Smith†

NASA Langley Research Center, Hampton, Virginia

Laminar hypersonic flow over spherical dome protuberances was analytically investigated to determine the increased pressure and heating loads to the surface. The configuration was mathematically modeled in a time-dependent three-dimensional analysis of the conservation of mass, momentum (Navier-Stokes), and energy equations. A boundary mapping technique was used to obtain a rectangular parallelepiped computational domain and a MacCormack explicit time-split predictor-corrector finite difference algorithm was used to obtain the solutions. Results show local pressures and heating rates for domes 0.5, 1, and 2 boundary-layer thicknesses high were increased by factors on the order of 1.4, 2, and 6, respectively. However, because leeward heating rates were reduced, the two lower height domes did not experience any net increase in total heat loads. The total heat load on the higher dome was increased by 25%. Flow over the lower dome was everywhere attached, while flow over the intermediate dome had small windward and leeward separations. The higher dome had an unsteady windward separation region and a large leeward separation region. Trailing vortices form on all domes, with the intensity increasing with the dome height. Discussions of applying the results to a thermally bowed thermal protection system are presented.

Nomenclature

c_v	= specific heat at constant volume
E	= total energy $[c_v T + \frac{1}{2}(u^2 + v^2 + w^2)]$
h	= dome height above flat plate
K	= thermal conductivity of air
k	= variable grid concentration parameter, Eq. (4)
p	= pressure
Q_T	= total heat load
q	= local heating rate
r	= radius measured from dome centerline
r_0	= radius of flat-plate/dome intersection
T	= temperature
T_{eq}	= equilibrium radiation temperature
t	= time
u, v, w	= velocity components
x, y, z	= coordinate directions
δ_{fp}	= flat-plate boundary-layer thickness at $x = x_c$
ϵ	= one-half the fillet width
ξ, η, ζ	= transformed coordinates
$\bar{\eta}$	= redistributed transformed coordinate, Eq. (4)
μ	= viscosity
ρ	= density
τ_{ij}	= stress tensor

Subscripts

c	= coordinate value at dome centerline
fp	= flat-plate value
max	= maximum coordinate value

Introduction

PROTUBERANCES in the form of large-diameter, small-height spherical domes often occur on hypersonic vehicles as a result of hardware design or thermal bowing. Hypersonic

flow over these protuberances produces increased local wall pressures and heating rates. Interest in this flow configuration and computation of the pressure and heating rate distributions on them has increased because of proposed alternative metallic thermal protection systems (TPS) to replace the fragile reusable surface insulation (RSI) on the original Space Shuttle.[1-3] Titanium and/or superalloy designs have been fabricated that are weight competitive with RSI and offer the advantages of mechanical fastening, longer life, and increased damage resistance. However, the use of metallic TPS introduces thermal bowing to the system, a physical phenomenon not present in the RSI system.[3] Bowing occurs because metals have relatively large coefficients of thermal expansion and TPS panels must sustain large temperature gradients through their thickness. This produces large thermal expansion in the outer portion of the panel and small thermal expansion in the inner portion of the panel. The square panels are held down at the corners, but otherwise the thermal expansion is unrestrained. As a result, the center of the panel bows out into the stream so that the vehicle moldline is altered. An array of panels takes on a quilted configuration.

Analyses of two-dimensional flow over a wavy wall are available in the literature; however, there are no analyses of three-dimensional flow over a configuration resembling the thermally bowed TPS. One study considering subsonic turbulent flow around a large bluff-body turret was recently reported.[4] While the flow conditions and body configurations are considerably different from those being considered here, the problems are formulated in a similar manner and both press the limits of the current vector-processing computers.

This preliminary study was undertaken to determine if the increased pressure and heating effects are significant and if the problem requires in-depth consideration. Thermally bowed panels were modeled by the generic configuration of spherical domes. Numerical gridding and computer storage limitations prohibited modeling an array of full-scale TPS panels, so a single row of 11.7 cm (4.6 in.) diameter domes was selected to be compatible with the gridding requirements. Dome heights of 0.25, 0.51, and 1.02 cm (0.1, 0.2, and 0.4 in.) were considered in a flowfield with a laminar boundary-layer thickness of 0.51 cm (0.2 in.). Freestream conditions were for Mach 7 flight at 36,576 m (120,000 ft) altitude. The analysis of this flow configuration will yield dimensionally similar

solutions. However, the proper balancing of the similarity parameters to ascertain that the small-scale processes in the boundary layer will fall into the similarity pattern requires additional analytical and experimental data not yet available.[5] Therefore, no extension of the results of this study to larger protuberances has been made.

The analysis used a three-dimensional formulation of the time-dependent equations for conservation of mass, momentum, and energy to model the flow. A MacCormack explicit time-split predictor-corrector finite difference algorithm was used to obtain a steady-state solution on Langley's Cyber 203 vector-processing computer. The results of those solutions are presented in this paper using state-of-the-art computer color graphics techniques.

A comprehensive experimental program to verify the results obtained in this analysis is scheduled for a later time. Some preliminary small-scale tests have provided qualitative correlation with some of the predicted phenomena. No experimental data will be presented in this paper.

Analysis

Governing Equations

Aerothermal loads on spherical domed protuberances were computed by mathematically modeling the flowfield with the continuum mechanics equations of motion. Air, the fluid medium, was modeled as a compressible, viscous, thermally conducting gas. Limiting assumptions include considering air as an isotropic, Newtonian ideal gas in local thermodynamic equilibrium. The three-dimensional, time-dependent system of differential equations describing this model include the conservation of mass, momentum (Navier-Stokes equations of motion), and energy. The constitutive relations for the thermodynamic state equation for an ideal gas and the Sutherland viscosity formula close the system. The differential equations have been derived in the literature[6] and are shown below written in short form,

$$\frac{\partial U}{\partial t} + \frac{\partial F}{\partial x} + \frac{\partial G}{\partial y} + \frac{\partial H}{\partial z} = 0 \qquad (1)$$

where

$$U = \begin{bmatrix} \rho \\ \rho u \\ \rho v \\ \rho w \\ \rho E \end{bmatrix} \qquad (1a)$$

$$F = \begin{bmatrix} \rho u \\ \rho uu - \tau_{11} \\ \rho uv - \tau_{12} \\ \rho uw - \tau_{13} \\ \rho Eu - K\frac{\partial T}{\partial x} - (u\tau_{11} + v\tau_{12} + w\tau_{13}) \end{bmatrix} \qquad (1b)$$

$$G = \begin{bmatrix} \rho v \\ \rho uv - \tau_{12} \\ \rho vv - \tau_{22} \\ \rho vw - \tau_{32} \\ \rho Ev - K\frac{\partial T}{\partial y} - (u\tau_{12} + v\tau_{22} + w\tau_{32}) \end{bmatrix} \qquad (1c)$$

$$H = \begin{bmatrix} \rho w \\ \rho uw - \tau_{13} \\ \rho vw - \tau_{23} \\ \rho ww - \tau_{33} \\ \rho Ew - K\frac{\partial T}{\partial z} - (u\tau_{13} + v\tau_{23} + w\tau_{33}) \end{bmatrix} \qquad (1d)$$

and where

$$\tau_{ij} = \delta_{ij}P - \mu \left(\frac{\partial W_i}{\partial X_j} - \frac{\partial W_j}{\partial X_i} - \frac{2}{3}\delta_{ij}\frac{\partial W_k}{\partial X_k} \right)$$

The physical domain of the problem, a series of domes on a flat plate, is shown in Fig. 1. Symmetry planes located at the center of each dome and between domes reduced the required model to one-half of a dome. The dome was specified by its height h above the flat plate and its radius r_0 at the dome/flat-plate intersection. The intersection between the dome and flat plate was made mathematically smooth by modeling a fillet region at $r_0 \pm \epsilon$ with a Hermite polynomial.

Boundary Conditions

A boundary-layer profile was input at the upstream boundary plane ($x=0$) and held constant throughout the computations. The input boundary-layer profile for Mach 7 flight at an altitude of 36,576 m (120,000 ft) was determined using a two-dimensional boundary-layer analysis[7] for laminar flow over a flat plate with a sharp leading edge. The resulting flat-plate boundary-layer height δ_{fp} at the center of the three-dimensional region ($x=x_c$) was 0.51 cm (0.2 in.). Dome heights 0.25, 0.51, and 1.02 cm (0.1, 0.2, and 0.4 in.) were investigated. The ratio of dome radius to boundary-layer height, r_0/δ_{fp}, was held constant at 11.5.

Both side boundaries were planes of symmetry on which the dependent variables were determined by quadratic extrapolation from interior points so that the cross-flow gradients $\partial/\partial z$ of all state variables were zero and the cross-flow velocity w was zero. The upper ($y=y_{max}$) and downstream ($x=x_{max}$) planes were specified as no-change boundaries, i.e., set equal to the plane next to them. The wall was a no-slip boundary with a constant temperature of 800 K (1440°R). This wall temperature is both the design temperature and the flat-plate radiation equilibrium temperature for the input boundary conditions of a titanium TPS, assuming a high-emittance coating and zero thermal diffusivity.

Computational Domain

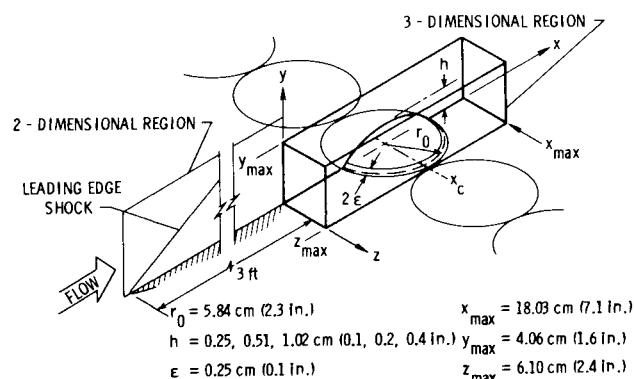A boundary-fitted coordinate system with the grid clustered in the boundary-layer region was formed with a two-

$r_0 = 5.84$ cm (2.3 in.) $x_{max} = 18.03$ cm (7.1 in.)

$h = 0.25, 0.51, 1.02$ cm (0.1, 0.2, 0.4 in.) $y_{max} = 4.06$ cm (1.6 in.)

$\epsilon = 0.25$ cm (0.1 in.) $z_{max} = 6.10$ cm (2.4 in.)

Fig. 1 Physical domain.

boundary grid-generation technique.[8] The physical domain, x,y,z (Fig. 1), was transformed into a rectangular parallelepiped computational domain, $\xi(x,y,z)$, $\eta(x,y,z)$, $\zeta(x,y,z)$, with uniform grid spacing utilizing the chain rule of differentiation, i.e., all spatial derivatives $\partial/\partial X_i$ were replaced by $\partial/\partial C_\ell$ $(\partial C_\ell/\partial X_i)$ where the C_ℓ for $\partial = 1,2,3$ are the transformed coordinates ξ,η,ζ. The resulting governing equation is

$$\frac{\partial U}{\partial t} + \frac{\partial \bar{F}}{\partial C_\ell}\frac{\partial C_\ell}{\partial X} + \frac{\partial \bar{G}}{\partial C_\ell}\frac{\partial C_\ell}{\partial y} + \frac{\partial \bar{H}}{\partial C_\ell}\frac{\partial C_\ell}{\partial z} = 0 \quad (2)$$

where $\bar{F}$, $\bar{G}$, and $\bar{H}$ are the transformed vectors F, G, and H [Eq. (1)].

The Jacobian matrix J required for the transformation

$$J = \frac{\partial C_I}{\partial X_j} = \begin{bmatrix} \dfrac{\partial \xi}{\partial x} & \dfrac{\partial \xi}{\partial y} & \dfrac{\partial \xi}{\partial z} \\[2mm] \dfrac{\partial \eta}{\partial x} & \dfrac{\partial \eta}{\partial y} & \dfrac{\partial \eta}{\partial z} \\[2mm] \dfrac{\partial \zeta}{\partial x} & \dfrac{\partial \zeta}{\partial y} & \dfrac{\partial \zeta}{\partial z} \end{bmatrix} \quad (3)$$
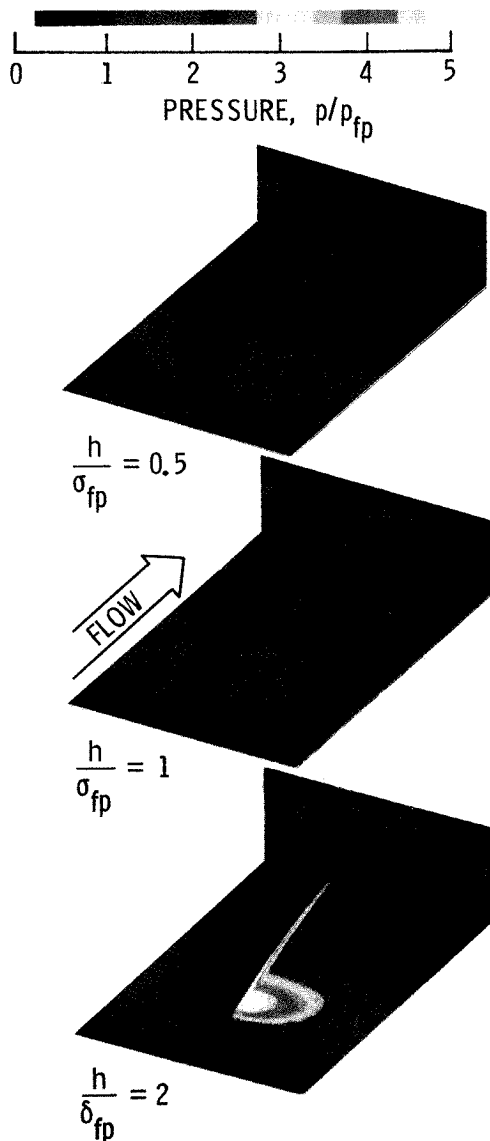

Fig. 2 Pressure distributions.

was determined by a linear mapping of the opposite boundaries of the computational domain onto the boundaries of the physical domain. In addition, increased resolution in the boundary-layer region was achieved by an exponential grid stretching in the η direction of the form,

$$\bar{\eta} = (e^{k\eta} - 1)/(e^k - 1) \quad (4)$$

where k is a free parameter that adjusts the grid spacing. The resulting connecting function in the y direction relating the computational domain to the physical domain is

$$y(\xi,\eta,\zeta) = Y(\xi,1,\zeta)\bar{\eta} + Y(\xi,0,\zeta)(1-\bar{\eta}) \quad (5)$$

where $Y(\xi,1,\zeta)$ and $Y(\xi,0,\zeta)$ are the upper and lower boundaries of the physical domain, respectively. The opposite boundaries in the x and z directions are plane and parallel; therefore, their connecting functions reduce to

$$x(\xi,\eta,\zeta) = x_{max}\xi$$
$$z(\xi,\eta,\zeta) = z_{max}\zeta \quad (6)$$

Differentiating these connecting functions and performing the necessary matrix inversion procedures produced the following constant terms for the Jacobian transformation matrix [Eq. (3)]:

$$\frac{\partial \xi}{\partial x} = \frac{1}{x_{max}}, \quad \frac{\partial \xi}{\partial y} = \frac{\partial \xi}{\partial z} = \frac{\partial \zeta}{\partial x} = \frac{\partial \zeta}{\partial y} = 0, \text{ and } \frac{\partial \zeta}{\partial z} = \frac{1}{z_{max}}$$

The relations for $\partial\eta/\partial x$, $\partial\eta/\partial y$, and $\partial\eta/\partial z$ (given in the Appendix) varied for the flat plate, fillet, and dome regions and were calculated and stored for each grid point in the domain.

Substituting the transform Jacobian into the short form of the equation system [Eq. (2)] reduced the system to

$$\frac{\partial U}{\partial t} + \frac{\partial \bar{F}}{\partial \xi}\frac{1}{x_{max}} + \frac{\partial \bar{F}}{\partial \eta}\frac{\partial \eta}{\partial x} + \frac{\partial \bar{G}}{\partial \eta}\frac{\partial \eta}{\partial y} + \frac{\partial \bar{H}}{\partial \eta}\frac{\partial \eta}{\partial z} + \frac{\partial \bar{H}}{\partial \zeta}\frac{1}{z_{max}} = 0 \quad (7)$$

The computational domain discretization,

$$0 \le \xi(i) \le 1 \text{ for } 1 \le i \le 64$$
$$0 \le \eta(j) \le 1 \text{ for } 1 \le j \le 32$$
$$0 \le \zeta(k) \le 1 \text{ for } 1 \le k \le 32$$

produced a field with 65,536 grid points and over 325,000 degrees of freedom.

Numerical Procedure

A finite difference solution to the governing equations was attained using the second-order-accurate MacCormack explicit time-split predictor-corrector algorithm.[9] The algorithm splits the differencing scheme into a series of one-dimensional operators. The operator in the principal flow direction, ξ, advances the computation by one time increment, while the operators in the other two coordinate directions, η and ζ, are divided into two steps of one-half a time increment each and applied symmetrically around the principle flow direction operator. This arrangement allows the principle flow direction operator to run at a Courant-Friedrichs-Lewy (CFL) number close to the optimum value of one. Each operator has two steps: a predictor step that advances the solution by its time increment based on a backward spatial differencing of the one-dimensional equations and a corrector step that recalculates the advancement based on a forward spatial differencing of the predicted results and averages the result
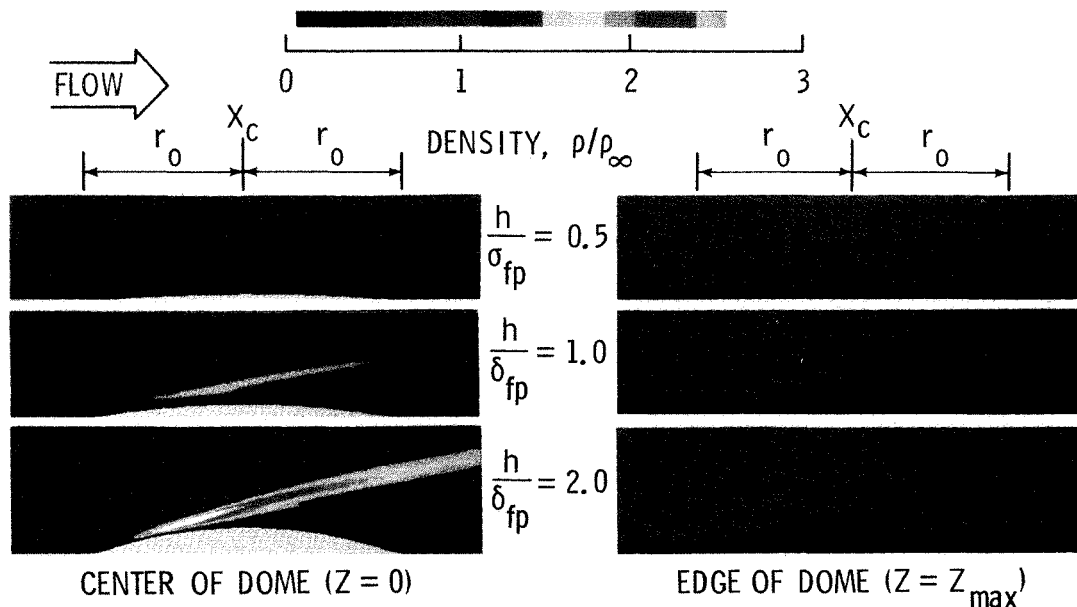
Fig. 3   Density distributions on longitudinal planes.

with the predictor. The predictor must therefore lag the corrector by a spatial increment in each coordinate direction. The combination of these two steps results in a second-order-accurate differencing scheme in time and space. A complete stability analysis of the algorithm is not available; however, the CFL limit yields a conservative time step.

In the formulation of this algorithm terms of order three and higher have been truncated. These terms are not significant in many flow regimes, but, they can be significant when modeling high-energy flowfields with strong shocks, as in this paper. In the region of a shock where the pressure gradients are extremely sharp, the higher-order terms act as dampers on the pressure disturbance. When these dampers are missing, as in most finite difference formulations, they can be simulated by adding terms such as the fourth-order eddy-viscosity-like term suggested in Ref. 10. The terms are added to the F, G, and H vectors [Eq. (1)] in both the predictor and corrector steps and are of significant magnitude only in regions where the pressure gradient is large. The solution was considered coverged to steady state when the flowfield parameters changed less than 0.01% per time step.

Programming and Computer Processing

The numerical procedure has been programmed to run on Langley's Cyber 203 vector-processing machine using 32-bit (half-word) arithmetic to provide increased speed and storage. Efficient vector processing with the large data base required an interleaved storage data management system (described in Ref. 8). A converged solution required approximately 1.9 h of processing time on the Cyber 203.

The validity and accuracy of the computer code was verified in Ref. 8 by reproducing the analytical results of Hung and MacCormack[11] for flow in a two-dimensional corner and the experimental results of Charwat and Redekopp[12] for flow in a symmetric wedge corner.

Results and Discussion

The effect of hypersonic flow over spherical domed protuberances was analyzed with a three-dimensional formulation of the mass, momentum, and energy equations. The results of the analysis are shown herein with the aid of computer color graphics displays and vector plots.
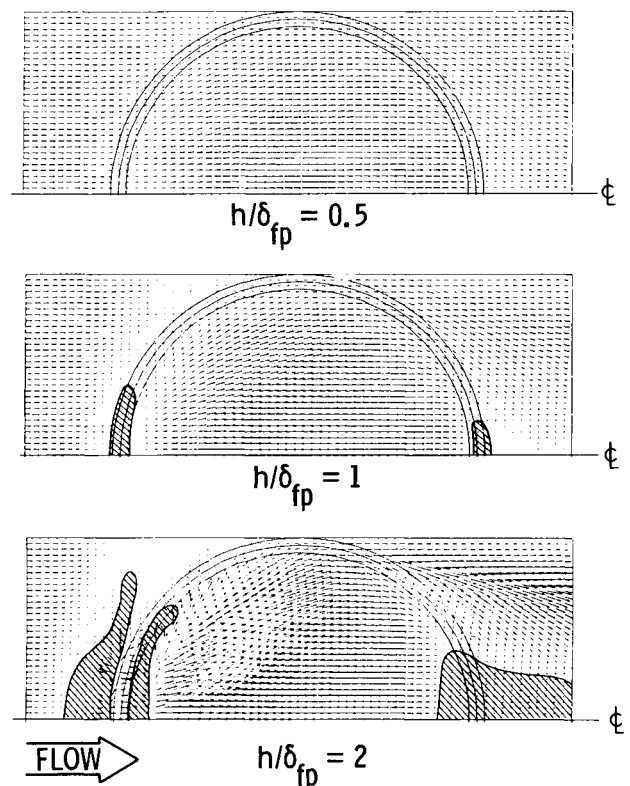

Fig. 4   Streamwise/cross-flow velocity vectors near the wall (cross-hatching indicates separated flow region).

Flowfield Perturbations

The effects of dome height on the flowfield pressure distributions are shown in Fig. 2. The isometric views show in one frame the wall ($y=0$), centerplane ($z=0$), and outflow boundary ($x=x_{max}$) pressure distributions—a total of over 5000 data points. Pressure variations were 0.34-6.21 kPa (0.05-0.90 psi) and the flat-plate wall pressure was 1.10 kPa (0.16 psi). Typically, the highest pressures occurred in the shock waves that formed on the windward side of the domes and increased exponentially with the dome height. The
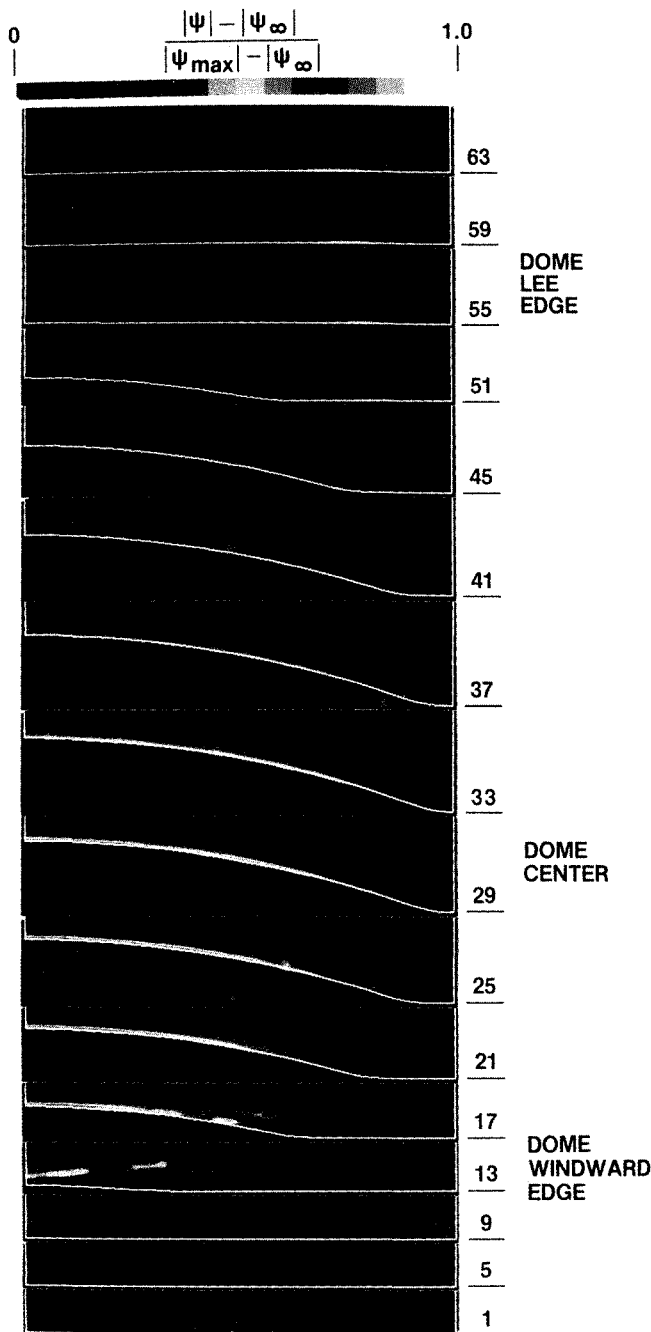
Fig. 5 Magnitude of vorticity vectors for $h/\delta_{fp} = 2$ (every fourth plane normal to the x direction).

Fig. 6 Heating rate distributions.

maximum wall pressures on the windward side for $h/\delta_{fp} = 0.5$, 1, and 2 were 1.52, 2.14, and 6.21 kPa (0.22, 0.31, and 0.90 psi), respectively. The curved shape of the shock waves are readily observed on the center and outflow planes. Expansion regions on the lee side of the domes had minimum wall pressures for $h/\delta_{fp} = 0.5$, 1, and 2 of 0.76, 0.55, and 0.34 kPa (0.11, 0.08, and 0.05 psi), respectively.

Density distributions down the centerplane of the dome ($z = 0$) and between the domes ($z = z_{max}$) are shown in Fig. 3. These distributions also show the shock and expansion regions, but more importantly they show the flowfield effects on the boundary-layer thickness. Planes at the center of the $h/\delta_{fp} = 1$ and 2 domes show weak shock waves generated ahead of the domes where the upstream influence of the adverse pressure gradient caused the boundary layer to grow. These weak upstream shocks merge with the stonger dome-generated shocks. The boundary-layer thickness was reduced
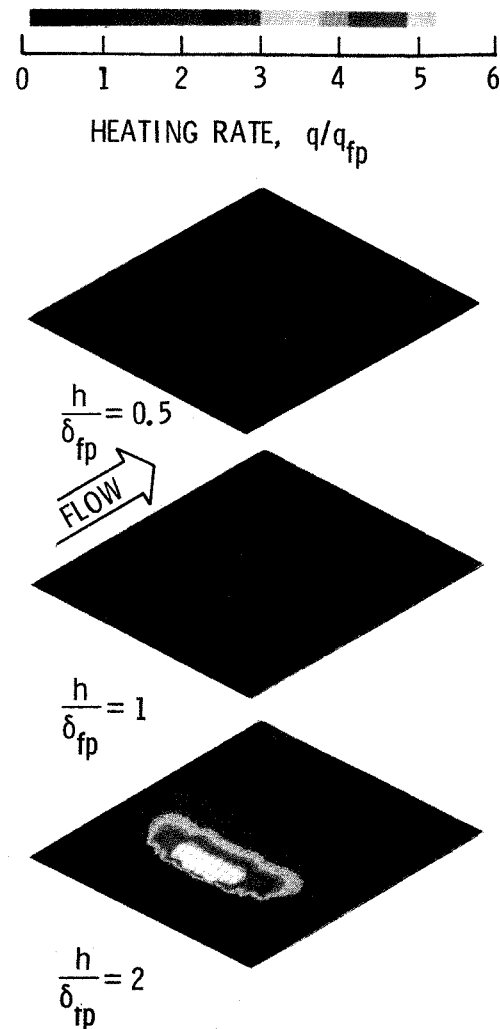
on the windward side of the dome by the strong shock/viscous-flow interaction, but grew rapidly in the leeward expansion region. As a result, the boundary layer on the downstream flat plate was significantly thicker than the entering plane boundary layer. Planes at the edge of the domes ($z = z_{max}$) show weak shock waves formed upstream of the channel minimum where the boundary layer began to grow. Here, the decreased upstream influence of the adverse pressure gradient was augmented by three-dimensional relief of flow around the dome to cause boundary-layer growth. Downstream of the minimum the boundary layer remained thick.

Vector plots of the streamwise/cross-flow velocity components one computational plane above the wall [approximately 0.02 cm (0.008 in.)] are shown in Fig. 4. The plot for $h/\delta_{fp} = 0.5$ shows that the flow next to the wall both on the windward and leeward sides of the dome and ahead of the channel minimum between the domes was decelerated, while the flow over the top of the dome was accelerated. Flow in the region of the quarter chord was diverted around the dome, while flow in the wake was diverted to the center expansion region behind the dome. The plot for flow over the $h/\delta_{hp} = 1$ dome shows similar, but more pronounced, features. In this case, small separated flow regions formed on both the windward and leeward sides of the dome. The $h/\delta_{fp} = 2$ dome had large separated flow regions with vector patterns that indicate strongly disturbed flow. The double separated flow region on the windward side of the dome experienced small time-dependent oscillations. The code remained stable despite the oscillations and the results suggest unsteady flow with the
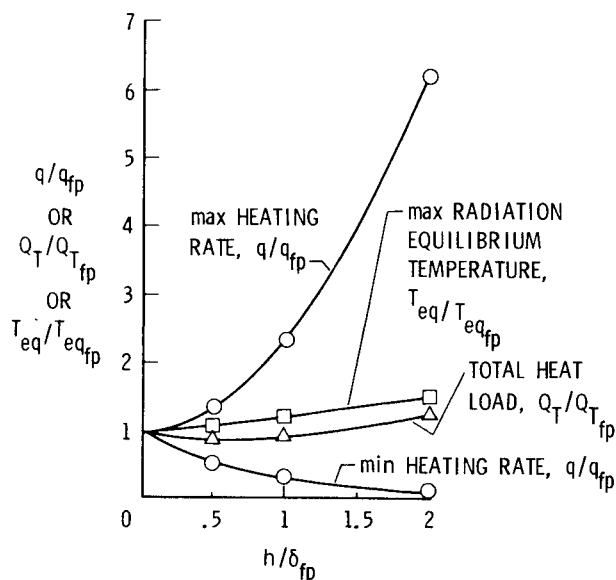
Fig. 7 Heating rate extremes, total heat load, and maximum radiation equilibrium temperatures.

separation region pulsating and shedding vortices. The mass of fluid involved in the process was small and there are no discernible effects on the downstream surface. The leeward separation region extended downstream a distance approximately equal to the dome radius and was totally captured in the computations by extending the region to 85 planes in the x direction.

Flowfield vorticity vector magnitudes for the $h/\delta_{fp} = 2$ dome are shown in Fig. 5. Every fourth plane in the x direction is shown for the pseudo-steady/state condition (when all transients except the previously mentioned small oscillations had dissipated). Vorticity was generated near the dome leading edge. Further downstream, discrete clumps of vorticity appear to have shed into the flowfield. The clumps rapidly diffused into the stream with no discernible effect on the surface. The unsteady vortex shedding could form von Kármán vortex streets, as seen in flow about cylinders,[6] and violate the symmetry plane assumptions. A solution admitting this possibility would require doubling the size of the physical domain and complicating the boundary conditions. Even if this could be practically accomplished, no measurable change in the wall pressure or heating rate is anticipated. Therefore, for the purpose of this study, the symmetry plane assumption was considered valid. Another region of high vorticity formed next to the wall as the flow expanded around the leeward side of the dome. These regions of vorticity also formed behind the smaller domes, but to a lesser extent.

Wall Heating Rate Perturbations

The effects of dome height on the surface heating rate distributions are shown in Fig. 6. The flat-plate heating rate was 18.50 kW/m^2 (1.63 Btu/ft$^2 \cdot$s) and the range of heating rates on the $h/\delta_{fp} = 2.0$ dome was 1.25-114.96 kW/m^2 (0.11-10.13 Btu/ft$^2 \cdot$s). Both the peak heating rate and the windward side area experiencing higher heating rates increased with the dome height. The trailing vortices caused increased heating on the leeward flat plate and the unsteady separated flow on the windward side of the $h/\delta_{fp} = 2.0$ dome caused the erratic heating pattern in that region. Reduced heating regions on the leeward side (except for vortex paths) and in the fillet and flat-plate regions appeared where the boundary-layer thickness had increased. The reduced heating region ahead of the dome moved further upstream as the dome height was increased.

The effects of the dome height on the minimum and maximum wall heating rates, total heat load, and maximum

radiation equilibrium temperature normalized by the flat-plate values are shown in Fig. 7. The maximum heating rate, like the maximum wall pressure, increased exponentially with the dome height. The total heat load (the integrated heating to the entire wall region shown in Fig. 6) for dome heights $h/\delta_{fp} = 0.5$ and 1 actually decreased by 14 and 8%, respectively, as a result of the large reduced heating area. The total heat load for $h/\delta_{fp} = 2$ was increased 25%. In applications such as passive TPS panels, the wall temperature is not constant but a function of the local thermal balance. An upper-limit wall temperature independent of the TPS physical design, material properties, and thickness can be found for a specified surface emissivity by assuming zero thermal diffusivity and a constant local heat-transfer coefficient and computing a radiation equilibrium temperature. These temperatures, corresponding to the maximum heating rates found on the domes, are shown in Fig. 7 normalized by the flat-plate radiation equilibrium temperature. The maximum temperature increased linearly with the dome height, but even the highest temperature 1170 K (2105°R) for $h/\delta_{fp} = 2$, was well below the 1820 K (3276°R) melting temperature of titanium. Local temperatures that exceed the design temperature will increase the thermal stresses and reduce the TPS fatigue life and will have to be taken into consideration in the design.

These results indicate that spherical domes higher than the local boundary-layer thickness cause significant disturbances in the flowfield and increase the local and total heating rates significantly. Dome heights less than the local boundary-layer thickness do not cause significant flowfield disturbances or increase the total heating loads, but do increase the local heating rates. However, this configuration represents the first TPS panel in an array. The boundary layer is thicker on the leeward side of the dome than on the windward side; therefore, downstream TPS panels should experience milder thermal loads than the leading panel, assuming that the downstream effects of the trailing vortices next to the wall are nominal. The downstream effects of the vortices are being investigated further.

If the spherical domes are the result of thermally bowed TPS panels, the variations in local heating rates will cause temperature gradients across the panels that will result in eccentric bowing, further increasing the heating on the windward side. The reactions of the panel are coupled to the design and materials in the panel. To accurately determine the performance of a thermally bowing TPS panel, a combined thermal/structural/aerothermal load analysis must be made. The results of this study show that thermal bowing could cause significant increases in local pressures and heating and emphasizes the need for a combined thermal structural analysis.

Conclusions

An analytical study of high-speed laminar flow over spherical dome protuberances was conducted to determine how the domes perturbed the flowfield and to determine the aerothermal heating to them. The flowfield was modeled as three-dimensional viscous flow utilizing the equations for conservation of mass, momentum, and energy. Dome heights of 0.5, 1, and 2 times the local boundary-layer thickness were investigated.

Results of the analysis show that shock waves were formed on all of the domes. For the middle and tallest domes, local windward side heating rates significantly increased (2.34 and 6.2 times the flat-plate value, respectively), flow separated, and downstream vortices formed. Total heat loads to domes less than or equal to the local boundary-layer height were not increased, but the total heat load to the tallest dome was increased by 25%.

If the domes are considered to model a thermally bowed TPS, the problem is coupled since the aerothermal load variations depend on the thermal-structural response and

must ultimately be studied as a combined thermal/structural/aerothermal load problem.

Appendix

The flat-plate, fillet, and dome regions of the spherical dome configuration are defined by the radius r on the $y=0$ plane measured from the dome centerline. The radius in terms of ξ and ζ is

$$r = \sqrt{(x_{max}\xi - x_c)^2 + (z_{max}\zeta)^2} \qquad (A1)$$

The Jacobian transform terms, $\partial/\partial x$, $\partial/\partial y$, and $\partial/\partial z$, for these areas are as follows:

Flat-plate region $[(r_0 + \epsilon) \leq r]$

$$\frac{\partial \eta}{\partial x} = \frac{\partial \eta}{\partial z} = 0, \quad \frac{\partial \eta}{\partial y} = \frac{e^k - 1}{y_{max} k e^{k\eta}} \qquad (A2)$$

Fillet region $[(r_0 - \epsilon) < r < (r_0 + \epsilon)]$ with

$$\beta = \frac{r - (r_0 - \epsilon)}{2\epsilon}, \quad 0 \leq \beta \leq 1$$

$$A = h - R + \sqrt{R^2 - (r_0 - \epsilon)^2}$$

$$B = \frac{\epsilon - 2(r_0 - \epsilon)}{\sqrt{R^2 - (r_0 - \epsilon)^2}}$$

$$R = (h^2 + r_0^2)/2h$$

$$D = \frac{[B(3\beta - 1) + 6A\beta](\beta - 1)}{y_{max} - (\beta - 1)^2 [A(2\beta + 1) + B\beta]}$$

$$\frac{\partial \eta}{\partial x} = -\left(\frac{e^{k(1-\eta)} - 1}{k}\right)\left(\frac{x_{max}\xi - x_c}{2r}\right)(D)$$

$$\frac{\partial \eta}{\partial \zeta} = \left(\frac{e^k - 1}{k e^{k\eta}}\right)\left(\frac{1}{y_{max} - (\beta - 1)^2[A(2\beta + 1) + B\beta]}\right)$$

$$\frac{\partial \eta}{\partial z} = -\left(\frac{e^{k(1-\eta)} - 1}{k}\right)\left(\frac{z_{max}\zeta}{2r}\right)(D) \qquad (A3)$$

Dome region $[r \leq (r_0 - \epsilon)]$ with

$$E = \frac{1}{\sqrt{R^2 - r^2}(y_{max} - h + R - \sqrt{R^2 - r^2})}$$

$$\frac{\partial \eta}{\partial x} = \left(\frac{e^{k(1-\eta)} - 1}{k}\right)(x_{max}\xi - x_c)(E)$$

$$\frac{\partial \eta}{\partial y} = \left(\frac{e^k - 1}{k e^{k\eta}}\right)\left(\frac{1}{y_{max} - h + R - \sqrt{R^2 - r^2}}\right)$$

$$\frac{\partial \eta}{\partial z} = \left(\frac{e^{k(1-\eta)} - 1}{k}\right)(z_{max}\zeta)(E) \qquad (A4)$$

References

[1]Kelly, H. N., Rummler, D.R., and Jackson, R. L., "Research in Structures and Materials for Future Space Transportation Systems —An Overview," AIAA Paper 79-0859, May 1979.

[2]Shideler, J. L., Kelly, H. N., Avery, D. E., Blosser, M. L., and Adelman, H. M., "Multiwall TPS—An Emerging Concept," *Journal of Spacecraft and Rockets*, Vol. 19, July-Aug. 1982, p. 358.

[3]Jackson, R. J. and Dixon, S. C., "A Design Assessment of Multiwall Metallic Stand-Off and RSI Reusable Thermal Protection System Including Space Shuttle Applications," NASA TM-81780, April 1980.

[4]Purohit, S. C., Shang, J. S., and Hankey, W. L. Jr., "Numerical Simulation of Flow around a Three-Dimensional Turret," *AIAA Journal*, Vol. 21, Nov. 1983, pp. 1533-1540.

[5]Reynolds, A. J., *Thermofluid Dynamics*, John Wiley & Sons, New York, 1971.

[6]Schlichting, H., *Boundary Layer Theory*, MacGraw-Hill Book Co., New York, 1968.

[7]Anderson, E. C. and Lewis, C. H., "Laminar or Turbulent Boundary-Layer Flows of Perfect Gases or Reacting Gas Mixtures in Chemical Equilibrium," NASA CR-1893, 1971.

[8]Smith, R. E., "Two-Boundary Grid Generations for the Solution of the Three-Dimensional Compressible Navier-Stokes Equations," NASA TM-83123, May 1981.

[9]MacCormack, R. W. and Paullay, A. J., "Computational Efficiency Achieved by Time Splitting of Finite Difference Operations," AIAA Paper 72-154, Jan. 1972.

[10]MacCormack, R. W. and Baldwin, B. S., "A Numerical Method for Solving the Navier-Stokes Equations with Application to Shock Boundary Interactions," AIAA Paper 75-1, Jan. 1975.

[11]Hung, C. and MacCormack, R., "Numerical Solution of Three-Dimensional Shock Wave and Turbulent Boundary Layer Interactions," *AIAA Journal*, Vol. 16, Oct. 1978, pp. 1090-1096.

[12]Charwat, A. F. and Redekopp, L. G., "Supersonic Interference Flow Along the Corner of Intersecting Wedges," RAND Corp., Men. RM-4863-PR [Contract AF49(638)-1700], July 1966.